Article

Exploring the Performance and Mass-Transfer Characteristics of Porous Zinc Anodes for Membraneless Hybrid-Flow Batteries

Lina Tang [1,†]**, Shuyang Dai** [1,†]**, Puiki Leung** [1,*]**, Mohd Rusllim Mohamed** [2]**, Yikai Zeng** [3,*]**, Xun Zhu** [1]**, Cristina Flox** [4] **, Akeel A. Shah** [1] **and Qiang Liao** [1]

[1] Key Laboratory of Low-Grade Energy Utilization Technologies and Systems, MOE, Chongqing University, Chongqing 400030, China; 20211001017@cqu.edu.cn (L.T.)

[2] Faculty of Electrical and Electronics Engineering Technology, Universiti Malaysia Pahang, Pekan 26600, Malaysia

[3] Institute of Engineering Thermophysics and New Energy, School of Mechanical Engineering, Southwest Jiaotong University, Chengdu 610032, China

[4] Institut de Ciencia de Materials de Barcelona, CSIC, Campus UAB, 08193 Barcelona, Spain; cflox@icmab.es

[*] Correspondence: p.leung@cqu.edu.cn (P.L.); ykzeng@swjtu.edu.cn (Y.Z.)

[†] These authors have contributed equally to this work.

Abstract: Zinc-based hybrid-flow batteries are considered as a promising alternative to conventional electrochemical energy-storage systems for medium- to large-scale applications due to their high energy densities, safety, and abundance. However, the performance of these batteries has been limited by issues such as dendritic growth and passivation of zinc anodes during charge–discharge cycling. To address this challenge, a variety of two- and three-dimensional zinc anodes have been investigated. While two-dimensional zinc anodes have been extensively studied, there has been limited investigation into three-dimensional zinc anodes for hybrid-flow batteries. This study highlights the potential of three-dimensional zinc anodes to mitigate overpotentials and improve the mass transport of active species to promote negative electrode reactions. The performance of a membraneless flow battery based on low-cost zinc and organic quinone was herein evaluated using experimental and numerical approaches. Specifically, the use of zinc fiber was shown to yield an average coulombic efficiency of approximately 90% and an average voltage efficiency of approximately 82% over the course of 100 cycles at a current density of 30 mA cm^{-2}. These results indicate the viability of using zinc fiber anodes to improve the performance of existing hybrid-flow batteries.

Keywords: electrochemical energy storage; zinc dendrite; organic quinone; two- and three-dimensional electrodes

1. Introduction

The rapid increase in population and economic development have led to an excessive dependence on fossil fuels, resulting in global energy and environmental challenges [1]. The deterioration of the environment and harm to human health brought on by greenhouse gases, toxic pollutants, and waste due to the usage of fossil fuels are becoming more and more significant [2]. As a result, it is anticipated that demand for power generation using renewable energy sources (such wind, biomass and solar power) would increase quickly in the next decades [3]. The intermittent and unstable nature of renewable energy sources, however, makes it difficult to sustain steady power levels. By facilitating the integration of renewable energy sources into the power grid, energy storage is thought to be useful in resolving this issue. This reduces greenhouse gas emissions and mitigates the consequences of climate change [4]. Admittedly, electrochemical energy storage is a highly efficient and versatile form of energy storage with rapid response times and no geographical limitations [5]. Examples of electrochemical storage technologies include lead–acid, lithium–ion, metal–air and redox-flow batteries. Among these, redox-flow batteries are particularly

well-suited for medium- and large-scale applications due to their unique architecture [6,7]. Unlike other batteries, redox-flow batteries store electrical energy in liquid electrolytes rather than electrodes. This architecture enables the decoupling of power and energy ratings, thereby enhancing its adjustability and scalability for various applications.

Over the past decades, redox-flow batteries have been developed based on both aqueous and non-aqueous electrolytes, each with their distinct properties. While aqueous batteries are limited by a relatively narrow electrochemical window of less than 1.6 V due to water electrolysis, they offer higher ionic conductivity and lower costs [8]. Currently, all successful redox-flow batteries installed at a MW scale are based on aqueous chemistries, specifically all-vanadium (100 MW/400 MW h, located in Dalian, China), zinc–bromine (2 MW/8 MW h, Queensland, Australia) and iron–chromium (10 MW/40 MWh, Mukawa, Japan). However, the costs of these systems are estimated to be between USD 200 and 600 (kW h)$^{-1}$, exceeding the target costs for widespread market penetration (i.e., USD < 100 (kW h)$^{-1}$) [9–12]. Nevertheless, among numerous cell components (electrolyte, gasket, flow frame, pump, and so on), membranes account for up to 40% of the overall cost of redox-flow battery systems, while electrolyte costs are not solely dependent on the expenses of the active materials but are also influenced by the cell voltages and multi-electron transfers [13,14]. Thus, new hybrid-flow batteries utilizing electronegative metal anodes are being explored as a cost-effective alternative to existing systems, especially those with membraneless architectures that arise when the direct interaction between the charged species is insignificant [15–17]. Among the metal anodes used in aqueous batteries, zinc has been widely used in rechargeable batteries due to its high volumetric capacity (5.85 Ah cm^{-3}) and negative electrode potential (−0.76 V vs. SHE) [18–20]. Several membraneless hybrid-flow batteries with zinc anodes have been developed, featuring positive electrode reactions such as solid-phase transformation, liquid-phase reaction, and metal-oxide electrodeposition in zinc–nickel [21], zinc–cerium [22], and zinc–manganese [17] systems, respectively. Meanwhile, the abundance and widespread availability of organic active materials from diverse sources have led to their increased attention [23,24]. As proposed by Leung et al., the integration of membraneless architecture, zinc anode, and organic active materials in aqueous hybrid-flow batteries has emerged as a practical approach to reach the target cost of less than USD 100 (kW h)$^{-1}$ [25].

Despite the effective use of flowing electrolytes, the main objective of this study was to assess the efficacy of the two- and three-dimensional zinc anodes for potential enhancement of existing hybrid-flow batteries considering the terrible dendrite of the zinc anode [26–28]. The increased surface areas of these three-dimensional anodes facilitate more uniform distribution and supply of active species to and from the electrolyte, mitigating localized regions with high current densities and subsequent pH elevation caused by hydrogen evolution [29–31]. In recent years, the research on 3D zinc–metal electrodes has made some progress in improving the effective deposition of metal anodes [32–38], but the mass-transfer behavior of 3D metal electrodes in non-membrane hybrid-flow batteries during charging and discharging is still unclear. Furthermore, for zinc-based membraneless hybrid-flow battery systems, the influence mechanism of the zinc anode structure and fluid dynamics on zinc deposition is not clear, and the transport and adsorption processes of zinc ions at the zinc anode interfaces with different structures need to be further studied.

In the literature, it is noteworthy that investigations into different forms of zinc anodes such as zinc foam and zinc fiber have been limited. This study represents a significant contribution to the field by evaluating these electrode materials through a combination of experimental and numerical approaches. The experimental characterizations included detailed analyses of the surface morphologies, crystal structures, and electrochemical behaviors of these electrodes, which were studied under flow-cell conditions using a scanning electron microscope, X-ray powder diffractometer, as well as half- and full-cell charge–discharge cycling. The results were facilitated by multiphysics models to understand the mass-transport phenomena within the membraneless hybrid -low batteries. The findings indicate that the three-dimensional electrodes (zinc fiber and foam) exhibited remarkable

performance in reducing electrode overpotentials and enhancing mass-transport processes. Notably, the use of zinc fibers as anodes in membraneless hybrid-flow batteries (Figure 1) demonstrated superior performance compared to planar electrodes, with coulombic and voltage efficiencies exceeding 80% after 50 cycles and showing a capacity retention of 90% after 100 cycles. These results provide valuable insights into the development of high-performance zinc anodes for next-generation zinc-based hybrid-flow battery systems.
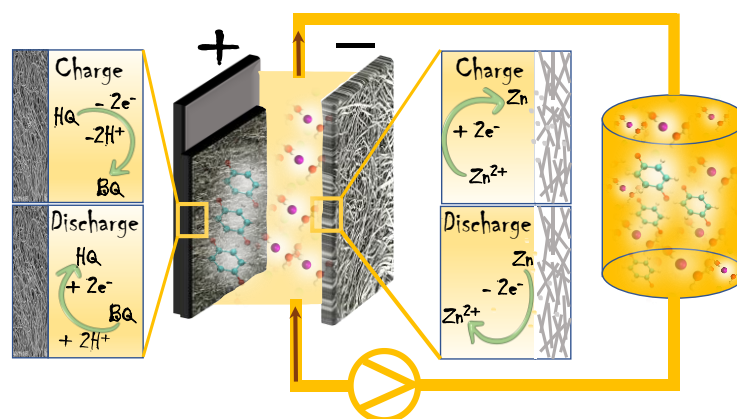
Figure 1. Schematic illustrations of the three-dimensional zinc fiber anode used in the membraneless zinc-based hybrid-flow batteries.

2. Experimental Details

2.1. Experimental Materials

The zinc negative electrodes used were of various forms, including two- and three-dimensional zinc, such as a high-purity zinc sheet (99.99% purity, Wanda Scientific Research Metal Material, Xingtai, China), mesh (1.25 mm × 2.5 mm, 99.85% purity, Lanrui Yingde Electrochemical New Material, Hengshui, China), foam (110 ppi, 99.99% purity, Kunshan Shangte New Material Co., Ltd, Kunshan, China.), and fiber (0.3 mm diameter, 99.9% purity, Green Steel Solana S.r.l., Italy). In order to facilitate readers to observe and understand the differences in the morphology and structure of the two-dimensional/three-dimensional zinc materials, large-sized optical photos are provided (Figure S4 in the Supplementary Materials). The carbon felt (SGL carbon, Germany, d = 3 mm) was used as the positive electrode. Prior to the experiments, all electrodes underwent a pretreatment process, which involved etching with 0.1 M hydrochloric acid to remove the surface oxide, degreasing with detergent, and cleaning in an ultrasonic bath.

Analytical-grade chemical reagents, including zinc chloride ($ZnCl_2$, 98% AR, Shanghai Yien Chemical Technology Company, Shanghai, China), hydroquinone (HQ, >99% AR, Beijing Jinming Biotechnology Co., Beijing, China), sodium chloride (NaCl, 99.8% GR, Shanghai Boer Chemical Reagents Co., Shanghai, China), and hydrochloric acid (HCl, 98% AR, Chengdu Colon Chemical Company, Chengdu, China), all without any additional purification, were used in the study. All solutions were prepared using de-ionized water with a resistivity of 18 MΩ cm.

2.2. Preparation of Zinc Anodes

The two- and three-dimensional zinc electrode materials used in the electrochemical tests were prepared by cutting and compressing them into the required size of 1 cm × 1 cm with a thickness of ca. 3 mm.

2.3. Physicochemical Characterizations

The wetting properties of the zinc anode materials were evaluated using a contact angle tester (XG-CAM, Shanghai xuanzhun instrument Co., Ltd., Shanghai, China). A sessile drop method was employed to measure the static contact angle between the zinc anode surface and a droplet of deionized water. A volume of 5 μL of deionized water was

dispensed onto the surfaces, and the contact angle was measured using an image-analyzing software.

The crystal structures of the zinc electrodes were analyzed using an X-ray powder diffractometer (Brucker D8 Advance, Germany) with Cu Kα radiation (λ = 0.15406 nm). The diffraction angle range was 10–90°, and the scanning speed was $10°$ min^{-1}. The XRD patterns were matched using the PDF2 card (Jade6.0) to determine the crystal structure and phase composition of the zinc anode materials. The crystallite sizes were calculated using the Scherrer equation (Equation (1) in the Supporting Information).

The surface morphologies were observed using a scanning electron microscope (SEM, TM-4000 Plus, Hitachi, Japan) operating at an acceleration voltage of 20 kV. SEM images were acquired at magnifications between $100\times$ and $2000\times$ to obtain high-resolution images of the surface features. The morphology and topography of zinc anodes were analyzed using a confocal laser scanning microscope (Brucker GT-X, Germany). This technique involved scanning a small area of the surface using a focused laser or electron beam and measuring the height or depth of each point to generate a three-dimensional map or contour for studying the surface characteristics and morphologies.

The thermogravimetric analysis and differential scanning calorimetry of the various samples were carried out using a differential thermogravimetric calorimetric analyzer (TGA-DSC Thermo plus EV02, Japan). The TGA-DSC curves were recorded from room temperature to 500 °C under N$_2$ atmosphere (50 cm^3 min^{-1}) at a heating rate of 10 °C min^{-1} to investigate the thermal stability, decomposition behavior, and weight loss of the samples. The particle sizes of the samples were estimated from the peak temperature of the exothermic reaction in the DSC curve, which was calculated using the Gibbs–Thomson equation (Equation (2) in the Supporting Information).
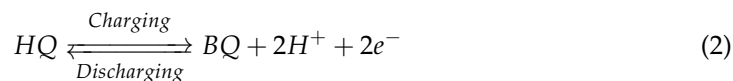
2.4. Half- and Full-Cell Charge–Discharge Cycling

The performances of the zinc anodes in both half- and full-cells were tested in a membraneless flow battery setup, which was previously utilized in our work [25]. The planar areas of both electrodes that were exposed to the electrolytes were maintained at 1 cm × 1 cm to ensure consistent reaction kinetics. In typical charge–discharge cycling, the primary electrode reactions for energy storage were zinc electrodeposition and the oxidation of 1,4-benzoquinone (BQ, from 1,4-hydroquinone), respectively (Equations (1) and (2)). Both of these reactions underwent two-electron transfer processes and were quasi-reversible. During the discharge process, these reactions were reversed to release electrical energy.

The following was performed at the negative electrode:

$$Zn^{2+} + 2e^- \underset{Discharging}{\overset{Charging}{\rightleftharpoons}} Zn \tag{1}$$
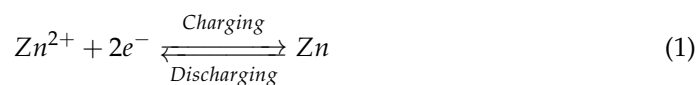
The following was performed at the positive electrode:

$$HQ \underset{Discharging}{\overset{Charging}{\rightleftharpoons}} BQ + 2H^+ + 2e^- \tag{2}$$

The electrolytes were prepared with de-ionized water and composed of 1 M zinc chloride (ZnCl$_2$) and 0.05 M hydroquinone (HQ) in 2.5 M sodium chloride (NaCl) and 0.1 M hydrochloric acid (0.1 M HCl, pH = 1.04). For accurate measurement and control of the electrochemical parameters, the electrochemical testing was carried out using a potentiostat (BP-300, Biologic, France). In order to evaluate the half-cell performance, a standard three-electrode configuration was used, where the working electrodes were the electrodes of interest (2D/3D zinc anodes). Counter and reference electrodes were made of platinum plate (1 cm^2) and Ag/AgCl, respectively. For full-cell testing, the counter electrode consisted of carbon felt for the positive electrode reactions.

For the open-circuit potential measurements, the electrode potentials of zinc anodes were continuously recorded in the electrolytes at 0% state of charge (SOC) for 10 min to determine the thermodynamic feasibility of their reaction at the electrode surface. Electrochemical impedance spectra (EIS) were recorded with a voltage amplitude of 10 mV at open-circuit voltages, with frequencies ranging from 0.1 to 10^6 Hz, to provide information about the electrochemical processes occurring at the electrode–electrolyte interface. For the Tafel measurements, the polarization curves were recorded by sweeping the electrode potentials between -1.2 and -0.8 V vs. Ag/AgCl at 5 mV s^{-1}. The exchange-current densities were then calculated using the Butler–Volmer equation (Equation 3 in Supporting Information) to evaluate the kinetic behavior of the anodes and to assess their suitability for hybrid-flow batteries.

Following this, the measurements of the electrode potentials of the zinc anodes and their corresponding polarization information were conducted in a hybrid-flow battery by increasing the charge and discharge current densities from 10 to 90 mA cm^{-2} (10–90 mA) with an interval of 10 mA for 2 min each (nine measurements in total). This range of current densities was chosen to capture the performance of the anodes under flowing conditions at 0% SOC. Unless otherwise stated, galvanostatic charge–discharge cycling was conducted at a constant current density of 30 mA cm^{-2} (30 mA) for durations of 0.25, 0.5, 1, 2, and 3 h. Following this, prolonged charge–discharge cycling was conducted at the same current density under a 15 min charge–15 min discharge regime to evaluate the stability and longevity of the anodes and to also obtain the overall performances of the full batteries. It is worth noting that all electrolytes were purged with nitrogen to remove air during the tests.

Additionally, the key performance indicators to evaluate the performance of hybrid-flow battery were introduced as follows:

Columbic efficiency (CE): The ratio of discharge capacity over charge capacity.

$$CE = \frac{I_{discharge} \times t_{discharge}}{I_{charge} \times t_{charge}} \tag{3}$$

Voltage efficiency (VE): The ratio of discharge voltage over charge voltage.

$$VE = \frac{V_{discharge}}{V_{charge}} \tag{4}$$

Energy efficiency (EE): The ratio of discharge energy over charge energy at a certain current density.

$$EE = \frac{I_{discharge} \times V_{discharge} \times t_{discharge}}{I_{charge} \times V_{charge} \times t_{charge}} = CE \times VE \tag{5}$$

Discharge capacity (Q): Discharge capacity stored in the total electrolyte.

$$Q = I_{discharge} \times t_{discharge} \tag{6}$$

2.5. COMSOL Multiphysics Numerical Modelling

In COMSOL multiphysics, numerical simulation studies are carried out for the hybrid-flow batteries composed of different zinc electrodes. In order to better research the mass-transfer process around different kinds of zinc electrodes inside the batteries, three-dimensional models of the batteries were made. For all zinc electrode models, the electrode area was 1 cm^2, and the electrode thickness was 3 mm. Except for the zinc plate, all the other zinc electrodes were constructed with a three-dimensional structure model. Related model equations are shown in the Supporting Information. Under reasonable circumstances, the following approximations are assumed:

(1)   The distance between the initial electrode and the deposited metal zinc is negligible;

(2) The electrodes are uniform in texture, and the structure of electrodes will not be changed by zinc deposition;

(3) The electrolyte has uniform viscosity and is an incompressible fluid, and its side reactions are negligible;

(4) Regardless of the gravity effect of the battery system, the battery operates in a stable state;

(5) The side reactions occurring on the electrode, such as the self-discharge reaction caused by direct contact between the metal zinc in the negative electrode and the electrolyte, are neglected.

3. Results and Discussions

3.1. Characterizations of Two- and Three-Dimensional Zinc Anodes

Crystal structure and morphology analyses of two- and three-dimensional zinc anodes in different forms were conducted using several characterization techniques. X-ray powder diffraction (Figure 2a) revealed a hexagonal phase (JCPDS No. 87-0713) and diffraction peaks corresponding to specific crystal planes in all zinc anodes despite variations in their morphologies and porosities [34,39,40]. Notably, the zinc mesh, zinc foam, and zinc fiber electrodes showed rightward shifts in peak positions compared to the zinc plate electrodes (local zoom-in X-ray powder diffraction patterns shown in Figure S2), indicating a decreased particle size and the potential for more reactive sites in these forms. Moreover, the mean particle size of zinc fiber was 47.754 nm, as calculated by the Scherrer equation, which was smaller than the zinc plate (63.816 nm), zinc mesh (49.375 nm), and zinc foam (48.941 nm), as summarized in Table S1. In particular, besides the zinc metal, there were a pair of diffraction peaks in the XRD pattern of Zn foam and fiber (45.0° and 52.2°, matching with Ni JCPDS No. 87-0712). The formation of crystallization phases in the zinc anodes was further evaluated using TGA-DSC thermal analysis (Figure 2b), showing exothermic peaks at ~421 °C for all the zinc plate, zinc mesh, zinc foam, and zinc fiber electrodes, with porous materials exhibiting a lower-temperature tendency. Following this, the Gibbs–Thomson equation can be used to determine the minimum particle size of the zinc fiber [29], which was consistent with XRD data (Table S1). Zinc fiber exhibits a high specific area, further enhancing the reactive area and hence lowering the electrode overpotentials. The SEM was used to examine the pore structures of the electrodes, revealing well-developed pore structures in zinc foam and zinc fiber, with a diameter of ca. 0.3 mm in zinc fiber, which is consistent with the manufacturer's specifications (Figure 2c). Furthermore, as shown in Figure S4, the unique features of 2D and 3D zinc anodes in relation to their surface texture, morphology, and porosity can be observed clearly. These factors play a crucial role in the overall performance and efficiency of the zinc-based hybrid-flow battery system.

Given the significant impact of the electrode–electrolyte interface on the electrode reaction processes of hybrid-flow batteries, the hydrophilicity of these zinc anodes was investigated using a contact angle tester [41–43]. The results presented in Figure 3a showed that zinc fiber had a low contact angle and a high affinity for water, promoting the electrodeposition and dissolution of zinc at the electrode–electrolyte interface during the charge–discharge processes. The optical images showed that the zinc mesh, zinc foam, and zinc fiber had varying degrees of porosity, with the zinc fiber having the most prominent porous structure (Figure S4). This structure increases the specific surface area of the zinc electrode material, expands the reactive area of the zinc negative electrode, and decreases the overpotential. Furthermore, a three-dimensional contour scan of the zinc fiber (Figure 3b) revealed that the surface of the zinc fiber was undulating and had a well-developed pore structure (with altitude intercepts up to 1145 μm) [39,44]. These structural analyses demonstrate that the porous zinc electrode, particularly the zinc fiber (zinc mesh, zinc foam, and zinc fiber), has an optimized electrode structure.
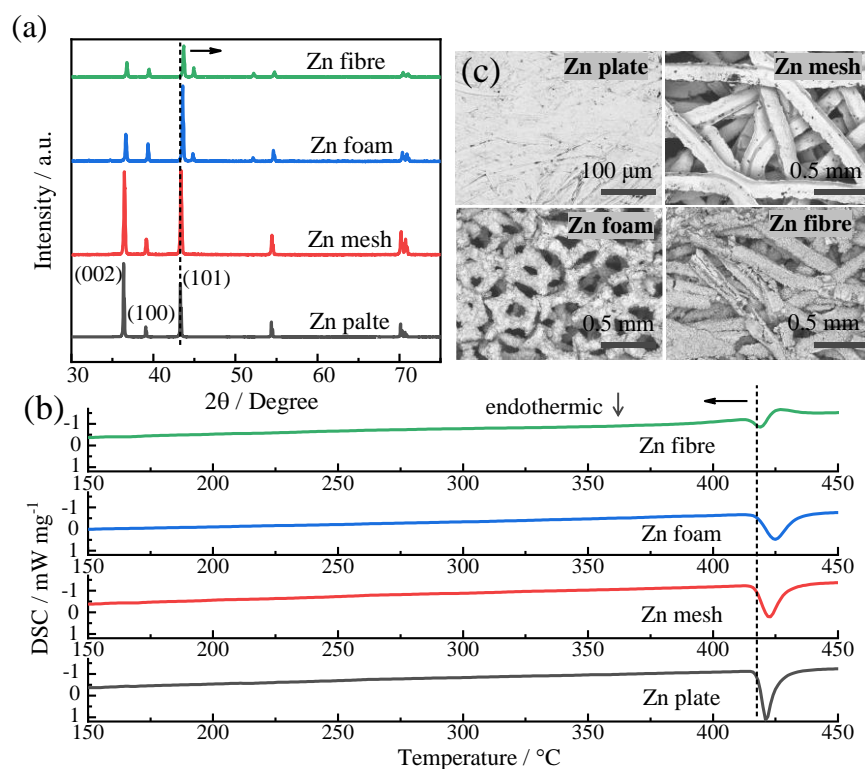
Figure 2. (**a**) X-ray diffraction patterns, (**b**) differential scanning calorimeter spectra analysis, and (**c**) SEM images of different zinc materials.
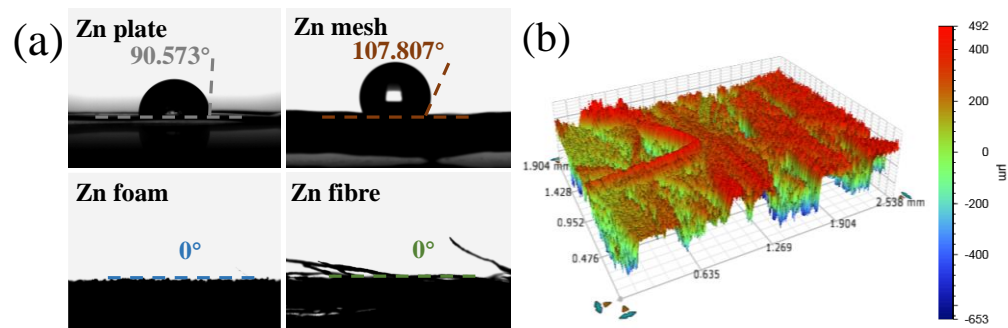

Figure 3. (**a**) Contact angles and (**b**) 3D reconstruction images for two- and three-dimensional zinc anodes.

3.2. Half-Cell Study of Zinc Anodes

The influences of the structural variations of two- and three-dimensional zinc anodes on the half-cell performances of hybrid-flow batteries were evaluated. In order to investigate the relationship between the structure and performance of the zinc metal electrode, a standard three-electrode system was employed to evaluate the performance of the zinc negative electrode half-cell. The working electrodes were zinc anodes of different forms, while platinum plate and Ag/AgCl (Sat. KCl) were used as the counter and reference electrodes, respectively.

The thermodynamic feasibility of the reduction reaction at the zinc anode surface was initially evaluated using open-circuit potential measurements. It is understood that the open-circuit potential is equivalent to the equilibrium potential, which depends on the thermodynamics of the electrode reactions under specific conditions. A negative shift in the equilibrium potential indicates that the reduction reaction is thermodynamically favored. As shown in Figure 4a, the porous zinc electrodes had more negative open-circuit potentials compared to the zinc plate, with the zinc fiber electrode exhibiting the most negative poten-

tial. This suggests that the reduction reaction processes were energetically more favorable for the porous zinc anodes, particularly the zinc fiber electrode. Moreover, the impedance spectroscopy characteristics of these anodes were analyzed at open-circuit potential to compare their reaction kinetics and resistances. The semi-circles in the Nyquist plot correspond to the charge-transfer resistance, which is a measure of the electron transfer kinetics at the electrode–electrolyte interface [45–48]. The Nyquist plot (Figure 4b) showed that the semi-circles of porous zinc electrodes such as zinc mesh, zinc foam, and zinc fiber were smaller than that of the zinc plate, indicating that these porous electrodes exhibited superior reaction kinetics and charge-transfer resistances at the electrode–electrolyte interface.
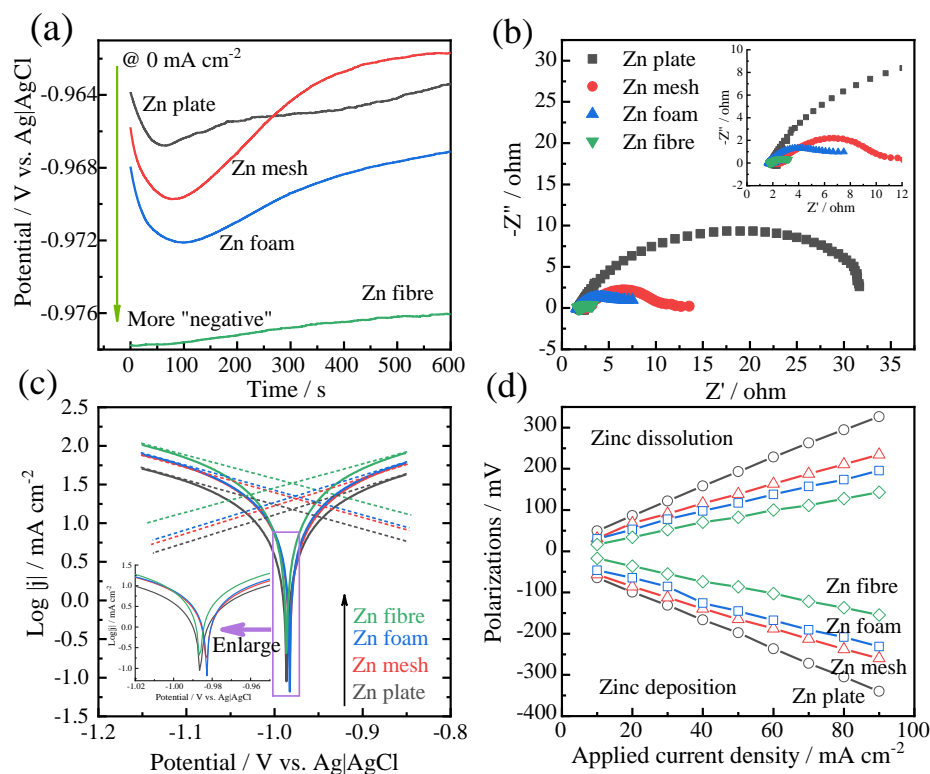

Figure 4. Electrochemical property analyses for all zinc materials (the black, red, blue and green lines present plate, mesh, foam and fibre, respectively). (**a**) The open-circuit potential, (**b**) the Nyquist plot, (**c**) the Tafel plot, and (**d**) the polarization potential at different current densities.

Tafel analyses were conducted to investigate the polarized conditions of these anodes for determining their kinetics at the electrode surface. By plotting the logarithm of the current density versus the applied potential (Figure 4c), the Tafel slope provides information about the activation energy of this particular electrochemical process. Since exchange-current density is a measure of the rate at which the redox reaction occurs at the electrode-electrolyte interface [28,38,49], it was observed that the porous zinc electrode exhibited higher exchange-current densities than the zinc plate. Based on the Butler–Volmer equation fitting the Tafel plot, the measured kinetic parameters, including exchange-current densities for zinc anodes, are summarized in Table S2. This can be attributed to the larger surface area and more porous structure of the zinc mesh, zinc foam, and zinc fiber electrodes, which provide more active sites for the electrochemical reaction, which was consistent with the results obtained from the open-circuit potential and impedance spectroscopy analyses. These findings may support the significant reduction in the electrode polarizations when these electrodes were equipped in a hybrid-flow battery under typical charge–discharge processes. Figure 4d shows the polarization values of these zinc anodes when the current densities increased from 10 to 90 mA cm^{-2} (10–90 mA), although these measurements also include the ohmic drop across the electrolytes. While the polarizations of all electrodes increased at higher current densities, the porous zinc anodes and zinc fiber exhibited

much less polarization than the zinc plate owing to their larger surface areas and better electrode–electrolyte interfaces.

The half-cell coulombic and voltage efficiencies of these anodes were further evaluated at a current density of 30 mA cm^{-2} through cycling for different charge–discharge durations (0.25, 0.5, 1, 2, and 3 h C-D), representing the state of charge of the batteries. Figure 5a presents the charge–discharge profiles (3 h C-D), indicating that all anodes demonstrated coulombic efficiencies of at least 99%. Meanwhile, it is obvious that the zinc fiber electrode had a higher voltage efficiency (90.8%) compared to the three other zinc electrodes (Zn plate 70.5%, Zn mesh 80.5%, and Zn foam 83.4%). As shown in Figure 5b, the half-cell efficiencies remained stable and unchanged over extended-charge or discharge durations. Regardless of the state of charge, the zinc fiber electrode exhibited the highest energy efficiency of ca. 90%, which can be attributed to both faster reaction kinetics and reduced electrode overpotentials, which is consistent with the results presented in Figure 4.
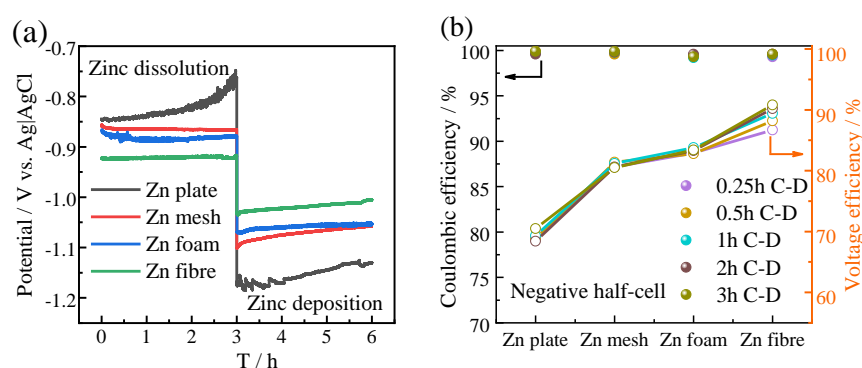
Figure 5. Performance analysis of half-cells with various two- and three-dimensional zinc negative electrodes (the black, red, blue and green lines present plate, mesh, foam and fibre, respectively). (**a**) Three hours C-D profiles and (**b**) the coulombic and voltage efficiencies at different states of charge. (The corresponding data values are listed in Tables S3 and S4.)

### 3.3. Full-Cell Study of a Membraneless Hybrid-Flow Battery

The previous sections of this study involved a detailed analysis and comparison of two- and three-dimensional zinc electrodes, which varied in their physical structures and half-cell performances. The results of the study demonstrated that the macro-microstructure of the zinc electrode plays a vital role in modifying and optimizing the electrode reaction process. Through the analysis of the anode materials, it was observed that porous electrodes, particularly the zinc fiber, exhibited superior electrode activity compared to other electrode materials. The superiority of porous zinc fiber can be attributed to its larger surface areas and better electrode–electrolyte interfaces, which facilitate the electrode reaction processes.

Based on these findings, a full-cell study was conducted to evaluate the feasibility of using porous zinc fiber electrodes in a novel, membraneless hybrid-flow battery based on low-cost zinc and organic active materials. Hydroquinone (HQ) was employed as the soluble active species for the positive electrode reactions at the initial state (discharged state). The primary objective of this study was to assess the potential enhancement of the performances of current hybrid-flow batteries by using porous zinc electrodes, supported by multiphysics models to enhance the understanding of the underlying mass-transport phenomena. The cycling performance of the full battery was evaluated through experimental tests. In addition, a full battery with a planar zinc plate anode was used for comparative analysis, similar to the porous electrodes, and corresponding test analyses were performed.

3.3.1. Mass-Transport Analysis Based on Multiphysics Models

In order to understand the mass-transport phenomena in hybrid-flow batteries, multiphysics models were employed to evaluate the electrolyte flow, by which the complex dynamics of the hybrid-flow battery system, including the distribution and velocity of active species (zinc ions and hydroquinone), were visualized and comprehended. Compared

with the traditional zinc plate electrode, the porous zinc electrode causes the electrolyte flow boundary layer to move inward towards the anode (as seen in Figure 6). The simulations revealed that the porous zinc anode, due to its porous structure, exhibited a significantly larger electrode reaction area compared to the zinc plate electrodes. However, this resulted in slower electrolyte flow passing through the channel at the negative electrode, likely due to the increased resistance of the porous material, which is consistent with previous studies of flow batteries using porous electrodes (e.g., carbon felts) [50]. Despite the sacrifice in mass transport, the large surface areas of the zinc fiber electrode still provided significant active sites for enabling efficient electrode reaction at reasonably high rates. Hence, it is essential to enhance the mass transport of the active species or increase the reaction sites at the electrode surfaces while maintaining the required electrode reaction rates.
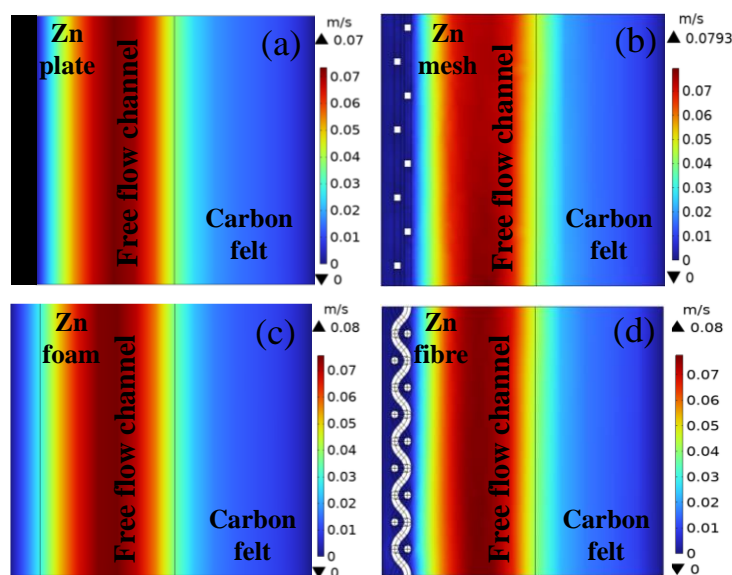

Figure 6. Velocity fields of a multiphysics model for full batteries equipped with zinc plate (**a**), zinc mesh (**b**), zinc foam(**c**) and zinc fibre (**d**) electrodes after 15 min charging (front view of cells).

It is known that increasing the electrolyte flow rate is a straightforward approach to enhance the mass transport in flow battery configuration [51]. However, this approach results in increased pumping power and a higher likelihood of leakage. In order to overcome these challenges, high-surface-area electrodes have garnered significant interest within the flow battery community as a means of ensuring efficient electrode reactions at higher current densities. Nevertheless, there is limited research on the use of such electrodes in hybrid-flow batteries, further justifying the evaluations of zinc fiber anodes in this study. Furthermore, by minimizing the direct reactions of charged species from the positive electrode with zinc anodes in a membraneless configuration, the active concentrations of the quinone species were kept at a low concentration of 0.05 M, highlighting the importance of its mass transport in this particular flow battery.

Figure 7 compares the influence of porous zinc electrodes on the concentration distribution of zinc ions with that of conventional zinc plates. As expected, the concentration distributions of zinc ions on the porous zinc electrodes interface, especially zinc fiber, were more homogeneous than that of the zinc plate, which greatly avoids the phenomenon of local over-polarization on the electrode surface and alleviates the corrosion of zinc anodes in the process of charge and discharge [30]. Notably, the concentration distributions of hydroquinone on the carbon felt–electrode interfaces exhibited a similar trend, and the concentration of HQ showed a lesser difference on the carbon felt–cathode interfaces for full cells equipped with zinc fiber anodes (Figure S6). Therefore, the use of the porous zinc anode facilitates the material transport of the electrolyte throughout the membrane-free hybrid-flow battery system, indicating favorable effects on electrode reactions. Despite

the advantages of using low concentrations of quinone species in minimizing the direct reactions of charged species from the positive electrode with zinc anodes, it should be noted that the concentration polarizations tend to be higher for the positive electrode reactions due to the depletion of hydroquinone in an electrolyte prepared with such a low concentration.
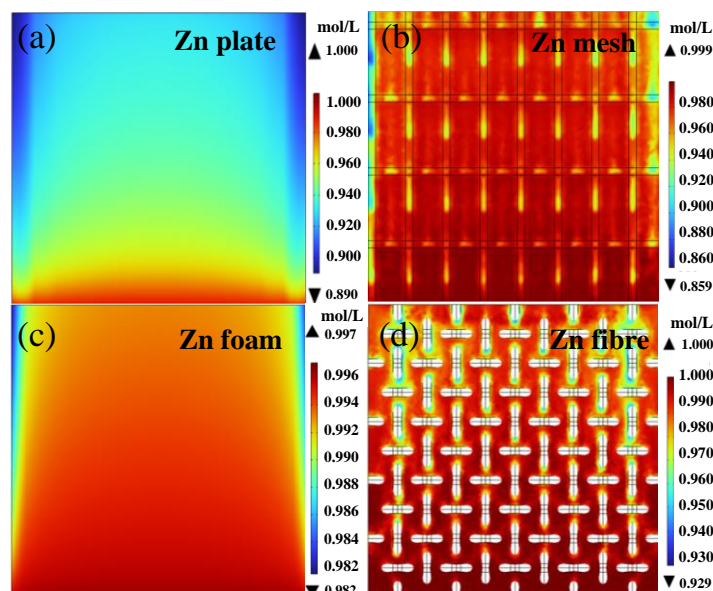
Figure 7. Concentration distribution of Zn^{2+} at the interfaces between zinc anodes and electrolyte solutions after 15 min charging (left view of cells): (**a**) zinc plate, (**b**) zinc mesh, (**c**) zinc foam and (**d**) zinc fibre.

3.3.2. Battery Performance Analyses

The performance of a full-cell, membraneless zinc-based battery was assessed using porous zinc and zinc plate anodes under galvanostatic charge–discharge cycling at a constant current density of 30 mA cm^{-2} under a 15 min charge–15 min discharge regime that was repeated over 100 cycles. The three batteries employing porous zinc anodes exhibited relatively high energy efficiencies during prolonged operation, as presented in Figures 8a,b and S7a,b. Among these, the full battery equipped with the zinc fiber anode demonstrated superior coulombic and voltage efficiencies, specifically 90% and 83%, respectively, compared to the zinc plate anode battery (92% and 60%). This advantage may arise from the zinc fiber electrode's larger surface area and better electrode–electrolyte interfaces, as explained in Sections 3.1 and 3.2. In particular, the decrease in the capacity of the zinc fiber anode can be observed to have attributed to shape changes that occur during prolonged charge–discharge cycling. Overall, the zinc fiber anode exhibited a capacity retention of 87% after 100 cycles, exceeding that of its zinc plate counterpart. Compared with the traditional zinc-based flow battery (Zn-Br and Zn-Fe flow battery system), the membraneless hybrid-flow battery proposed in this paper has a lower capital cost (USD 136 per kWh) and a competitive battery performance (Table S5). This result suggests the stability and durability of the zinc fiber anodes, which are effective for prolonged cycling performances. These findings indicate the viability of utilizing zinc fiber as a three-dimensional anode for hybrid-flow batteries, underscoring its advantages in mass transfer and electrode kinetics, which leads to an enhanced charge–discharge performance and long-term stability. Future studies may focus on optimizing the zinc fiber electrode's structure and composition to further improve its performance and assess its potential in other electrochemical systems.
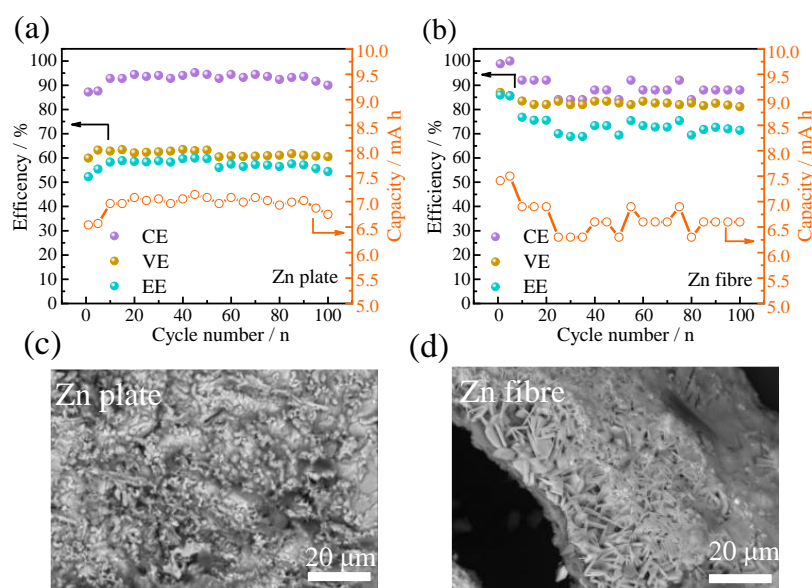
Figure 8. Comparison of the system efficiencies and capacities of the full batteries equipped with zinc plate (**a**) and zinc fiber anodes (**b**) at 30 mA cm^{-2}; the surface morphology of the zinc plate anode (**c**) and zinc fiber anode (**d**) after 100 cycles of charging–discharging.

In order to further understand the relationship between the surface depositions of zinc ions and the battery performance, the surface constructures of the zinc anodes were observed by scanning electron microscope after cycles of charging–discharging (Figures 8c,d and S7c,d). As shown in Figure 8c, the surface of the zinc plate after 100 cycles of charging–discharging was full of wrinkles and nodes. On the other hand, the surfaces of the porous zinc electrodes were ordered with deposited zinc particles with different particle sizes after continuous charge and discharge cycles. Therefore, the shape and surface structure of the zinc anode play an important role in the nucleation and crystallization process of zinc ions, and the porous zinc electrode structure can effectively alleviate the formation of zinc dendrites.

4. Conclusions

The present study investigated the performance of different types of two- and three-dimensional zinc anodes in hybrid-flow batteries and characterized their electrochemical and structural properties using various techniques. The findings revealed that porous zinc anodes, particularly zinc fiber, possess superior electrode structures with well-developed pore structures and larger specific surface areas, which enhance the reactive area and demonstrate superior reaction kinetics and charge-transfer resistances at the electrode–electrolyte interface. Half- and full-cell studies were conducted to evaluate the feasibility of using porous zinc fiber electrodes in a membraneless hybrid-flow battery, and the findings were supported by multiphysics models to understand the underlying electrolyte flow and mass-transport phenomena. Although the zinc fiber anode exhibited a large surface area with significant active sites for efficient electrode reactions, it resulted in a slower electrolyte flow passing through the negative electrode channel. Full-battery performance was assessed by comparing porous zinc fiber with a conventional zinc plate anode under galvanostatic charge–discharge cycling at 30 mA cm^{-2}. Attributed to the larger surface area and better electrode–electrolyte interfaces, the zinc-fiber-anode-equipped battery showed superior energy efficiency (EE), approximately 75% greater than 50% of the zinc plate. Moreover, the zinc fiber anode exhibited an 87% capacity retention after 100 cycles, demonstrating its adequate stability and durability for extended periods of use. However, there are some challenges/shortcomings regarding using Zn fiber anodes in commercial applications. One significant challenge is the stability and shape change of the zinc fibers

during prolonged cycling, which can result in reduced porosity and surface area, ultimately impacting the long-term stability and performance of the anode. Another critical aspect is the potential dissolution of zinc fibers, particularly under high acid concentrations and elevated temperatures. Rapid fiber dissolution can lead to a decrease in the overall capacity and life cycle of the anode. In order to tackle these challenges, optimizing electrode materials and electrolyte composition should be achieved by investigating different fiber morphologies and coatings that enhance the stability and shape retention during cycling. Moreover, future research may include the use of advanced characterization techniques such as in situ and operando measurements to provide deeper insights into the reaction mechanisms and kinetics in porous zinc anodes. These efforts will contribute to unlocking the full potential of hybrid-flow batteries as a promising energy-storage solution for a wide range of applications.

Supplementary Materials: The following supporting information can be downloaded at: https://www.mdpi.com/article/10.3390/batteries9070340/s1, Figure S1: Schematic of three-dimensional hybrid flow batteries models: (a) zinc plate electrode battery; (b) zinc fibrer electrode battery; Figure S2: The local zoom-in X-ray powder diffraction patterns for different zinc materials; Figure S3: The time–heat flow pattern for zinc plate; Figure S4: The optical images for different zinc electrodes; Figure S5: The short-time charging–discharging profiles to evaluate polarization potentials for different zinc electrodes; Figure S6: Concentration distribution of HQ at the interfaces between zinc electrodes and electrolyte solutions after 15 min charging (right view of cells); Figure S7: Comparison of the system efficiencies and capacities of the full batteries equipped with zinc mesh (a) and zinc foam anodes (b) at 30 mA cm^{-2}; the surface morphology of the zinc mesh anode (c) and zinc foam anode (d) after 100 cycles of charging–discharging; Figure S8: (a) Constant-current long-cycle charge–discharge curves; (b) charge–discharge profiles at the 4th cycle; (c) charge–discharge profiles at the 50th cycle for the full batteries equipped with zinc anodes; (d) charge–discharge profiles for the full batteries equipped with zinc fiber anode at the 4th, 50th, and 100th cycles, respectively; Figure S9: The validation of the COMSOL multiphysics model with experimental data. (a) Zinc plate, (b) zinc mesh, (c) zinc foam, and (d) zinc fiber; Table S1: The calculation results of the mean crystallite size based on XRD (crystal plane (002)) and DSC for zinc materials; Table S2: Measured kinetic parameters for 2D/3D zinc anodes from Butler–Volmer fit to Tafel slope; Table S3: The half-cell coulombic efficiencies at different states of charge for 2D/3D zinc anodes; Table S4: The half-cell voltage efficiencies at different states of charge for 2D/3D zinc anodes; Table S5: A summary of battery performance and capital cost for relevant aqueous conventional and zinc-based RFBs. References [52,53] are cited in the supplementary materials.

References

1. Zhang, H.; Hao, R.; Liu, X.; Zhang, N.; Guo, W.; Zhang, Z.; Liu, C.; Liu, Y.; Duan, C.; Qin, J. Thermodynamic performance analysis of an improved coal-fired power generation system coupled with geothermal energy based on organic Rankine cycle. *Renew. Energy* **2022**, *201*, 273–290. [CrossRef]
2. Song, Y.L.K.; Zhang, X.; Jiang, J.; Sun, C.; Lan, H. A Review on Interoperability of Wireless Charging Systems for Electric Vehicles. *Energies* **2023**, *16*, 1653. [CrossRef]
3. Chu, S.; Cui, Y.; Liu, N. The path towards sustainable energy. *Nat. Mater.* **2016**, *16*, 16–22. [CrossRef] [PubMed]
4. Rahman, M.A.; Kim, J.H.; Hossain, S. Recent advances of energy storage technologies for grid: A comprehensive review. *Energy Storage* **2022**, *4*, e322. [CrossRef]
5. Gür, T.M. Review of electrical energy storage technologies, materials and systems: Challenges and prospects for large-scale grid storage. *Energy Environ. Sci.* **2018**, *11*, 2696–2767. [CrossRef]
6. Emmett, R.K.; Roberts, M.E. Recent developments in alternative aqueous redox flow batteries for grid-scale energy storage. *J. Power Sources* **2021**, *506*, 230087. [CrossRef]
7. Schubert, C.; Hassen, W.F.; Poisl, B.; Seitz, S.; Schubert, J.; Usabiaga, E.O.; Gaudo, P.M.; Pettinger, K.-H. Hybrid Energy Storage Systems Based on Redox-Flow Batteries: Recent Developments, Challenges, and Future Perspectives. *Batteries* **2023**, *9*, 211. [CrossRef]
8. Tang, L.; Leung, P.; Xu, Q.; Mohamed, M.R.; Dai, S.; Zhu, X.; Flox, C.; Shah, A.A. Future perspective on redox flow batteries: Aqueous versus nonaqueous electrolytes. *Curr. Opin. Chem. Eng.* **2022**, *37*, 100833. [CrossRef]
9. Mongird, V.V.K.; Alam, J.; Vartanian, C.; Sprenkle, V.; Baxter, R. Grid Energy Storage Technology Cost and Performance Assessment. *Energy* **2020**, *5*, 6–15.
10. Brushett, F.R.; Aziz, M.J.; Rodby, K.E. On Lifetime and Cost of Redox-Active Organics for Aqueous Flow Batteries. *ACS Energy Lett.* **2020**, *5*, 879–884. [CrossRef]
11. Zhang, H.; Sun, C.; Ge, M. Review of the Research Status of Cost-Effective Zinc–Iron Redox Flow Batteries. *Batteries* **2022**, *8*, 202. [CrossRef]
12. Sun, H.Z. C-Y. Investigation of Nafion series membranes on the performance of iron-chromium redox flow battery. *Int. J. Energy Res.* **2019**, *43*, 8739–8752. [CrossRef]
13. Tang, L.; Leung, P.; Mohamed, M.R.; Xu, Q.; Dai, S.; Zhu, X.; Flox, C.; Shah, A.A.; Liao, Q. Capital cost evaluation of conventional and emerging redox flow batteries for grid storage applications. *Electrochim. Acta* **2023**, *437*, 141460. [CrossRef]
14. Pahlevaninezhad, M.; Leung, P.; Velasco, P.Q.; Pahlevani, M.; Walsh, F.C.; Roberts, E.P.L.; de Le, C.P. A nonaqueous organic redox flow battery using multi-electron quinone molecules. *J. Power Sources* **2021**, *500*, 229942. [CrossRef]
15. Yadav, G.G.; Weiner, M.; Upreti, A.; Huang, J.; Lambert, T.N.; Arnot, D.J.; Schorr, N.B.; Bell, N.S.; Turney, D.; Hawkins, B.; et al. The advent of membrane-less zinc-anode aqueous batteries with lithium battery-like voltage. *Mater. Horiz.* **2022**, *9*, 2160–2171. [CrossRef] [PubMed]
16. Sánchez-Díez, E.; Ventosa, E.; Guarnieri, M.; Trovò, A.; Flox, C.; Marcilla, R.; Soavi, F.; Mazur, P.; Aranzabe, E.; Ferret, R. Redox flow batteries: Status and perspective towards sustainable stationary energy storage. *J. Power Sources* **2021**, *481*, 228804. [CrossRef]
17. Zhang, H.; Cheng, Y.; Lek, D.G.; Liu, T.; Lin, F.; Luo, W.; Huang, S.; Gao, M.; Wang, X.; Zhi, Y.; et al. Membrane-free redox flow cell based on thermally regenerative electrochemical cycle for concurrent electricity storage, cooling and waste heat harnessing of perovskite solar cells. *J. Power Sources* **2022**, *548*, 232081. [CrossRef]
18. Ma, L.; Zhi, C. Zn electrode/electrolyte interfaces of Zn batteries: A mini review. *Electrochem. Commun.* **2021**, *122*, 106898. [CrossRef]
19. Lu, W.; Zhang, C.; Zhang, H.; Li, X. Anode for Zinc-Based Batteries: Challenges, Strategies, and Prospects. *ACS Energy Lett.* **2021**, *6*, 2765–2785. [CrossRef]
20. Yuan, Z.; Yin, Y.; Xie, C.; Zhang, H.; Yao, Y.; Li, X. Advanced Materials for Zinc-Based Flow Battery: Development and Challenge. *Adv. Mater.* **2019**, *31*, e1902025. [CrossRef]
21. Cheng, J.; Zhang, L.; Yang, Y.-S.; Wen, Y.-H.; Cao, G.-P.; Wang, X.-D. Preliminary study of single flow zinc–nickel battery. *Electrochem. Commun.* **2007**, *9*, 2639–2642. [CrossRef]
22. Leung, P.; de Le, C.P.; Walsh, F.C. An undivided zinc–cerium redox flow battery operating at room temperature (295 K). *Electrochem. Commun.* **2011**, *13*, 770–773. [CrossRef]
23. Kong, T.; Liu, J.; Zhou, X.; Xu, J.; Xie, Y.; Chen, J.; Li, X.; Wang, Y. Stable Operation of Aqueous Organic Redox Flow Batteries in Air Atmosphere. *Angew. Chem. Int. Ed.* **2023**, *62*, e202214819. [CrossRef] [PubMed]
24. Fan, H.; Hu, B.; Li, H.; Ravivarma, M.; Feng, Y.; Song, J. Conjugate-Driven Electron Density Delocalization of Piperidine Nitroxyl Radical for Stable Aqueous Zinc Hybrid Flow Batteries. *Angew. Chem. Int. Ed.* **2022**, *61*, e202115908. [CrossRef] [PubMed]
25. Leung, P.; Martin, T.; Shah, A.A.; Mohamed, M.R.; Anderson, M.A.; Palma, J. Membrane-less hybrid flow battery based on low-cost elements. *J. Power Sources* **2017**, *341*, 36–45. [CrossRef]
26. Hao, J.; Li, X.; Zhang, S.; Yang, F.; Zeng, X.; Zhang, S.; Bo, G.; Wang, C.; Guo, Z. Designing Dendrite-Free Zinc Anodes for Advanced Aqueous Zinc Batteries. *Adv. Funct. Mater.* **2020**, *30*, 2001263. [CrossRef]
27. Han, D.; Wu, S.; Zhang, S.; Deng, Y.; Cui, C.; Zhang, L.; Long, Y.; Li, H.; Tao, Y.; Weng, Z.; et al. A Corrosion-Resistant and Dendrite-Free Zinc Metal Anode in Aqueous Systems. *Small* **2020**, *16*, e2001736. [CrossRef]

28. Yang, Q.; Li, Q.; Liu, Z.; Wang, D.; Guo, Y.; Li, X.; Tang, Y.; Li, H.; Dong, B.; Zhi, C. Dendrites in Zn-Based Batteries. *Adv. Mater.* **2020**, *32*, e2001854. [CrossRef]

29. Chamoun, M.; Hertzberg, B.J.; Gupta, T.; Davies, D.; Bhadra, S.; Van Tassell, B.; Erdonmez, C.; Steingart, D.A. Hyper-dendritic nanoporous zinc foam anodes. *NPG Asia Mater.* **2015**, *7*, e178. [CrossRef]

30. Cai, Z.; Wang, J.; Sun, Y. Anode corrosion in aqueous Zn metal batteries. *eScience* **2023**, *3*, 100093. [CrossRef]

31. Borchers, N.; Clark, S.; Horstmann, B.; Jayasayee, K.; Juel, M.; Stevens, P. Innovative zinc-based batteries. *J. Power Sources* **2021**, *484*, 229309. [CrossRef]

32. Guo, N.; Huo, W.; Dong, X.; Sun, Z.; Lu, Y.; Wu, X.; Dai, L.; Wang, L.; Lin, H.; Liu, H.; et al. A Review on 3D Zinc Anodes for Zinc Ion Batteries. *Small Methods* **2022**, *6*, e2200597. [CrossRef]

33. Hopkins, B.J.; Sassin, M.B.; Chervin, C.N.; DeSario, P.A.; Parker, J.F.; Long, J.W.; Rolison, D.R. Fabricating architected zinc electrodes with unprecedented volumetric capacity in rechargeable alkaline cells. *Energy Storage Mater.* **2020**, *27*, 370–376. [CrossRef]

34. Huang, Z.; Li, Z.; Wang, Y.; Cong, J.; Wu, X.; Song, X.; Ma, Y.; Xiang, H.; Huang, Y. Regulating Zn(002) Deposition toward Long Cycle Life for Zn Metal Batteries. *ACS Energy Lett.* **2022**, *8*, 372–380. [CrossRef]

35. Li, H.; Zhang, W.; Elezzabi, A.Y. Transparent Zinc-Mesh Electrodes for Solar-Charging Electrochromic Windows. *Adv. Mater.* **2020**, *32*, e2003574. [CrossRef]

36. Parker, J.F.; Chervin, C.N.; Nelson, E.S.; Rolison, D.R.; Long, J.W. Wiring zinc in three dimensions re-writes battery performance—Dendrite-free cycling. *Energy Environ. Sci.* **2014**, *7*, 1117–1124. [CrossRef]

37. Parker, J.F.; Nelson, E.S.; Wattendorf, M.D.; Chervin, C.N.; Long, J.W.; Rolison, D.R. Retaining the 3D framework of zinc sponge anodes upon deep discharge in Zn-air cells. *ACS Appl. Mater. Interfaces* **2014**, *6*, 19471–19476. [CrossRef]

38. Xue, R.; Kong, J.; Wu, Y.; Wang, Y.; Kong, X.; Gong, M.; Zhang, L.; Lin, X.; Wang, D. Highly reversible zinc metal anodes enabled by a three-dimensional silver host for aqueous batteries. *J. Mater. Chem. A* **2022**, *10*, 10043–10050. [CrossRef]

39. Zhao, R.; Dong, X.; Liang, P.; Li, H.; Zhang, T.; Zhou, W.; Wang, B.; Yang, Z.; Wang, X.; Wang, L.; et al. Prioritizing Hetero-Metallic Interfaces via Thermodynamics Inertia and Kinetics Zincophilia Metrics for Tough Zn-Based Aqueous Batteries. *Adv. Mater.* **2023**, *35*, e2209288. [CrossRef]

40. Zeng, Y.; Sun, P.X.; Pei, Z.; Jin, Q.; Zhang, X.; Yu, L.; Lou, X.W.D. Nitrogen-Doped Carbon Fibers Embedded with Zincophilic Cu Nanoboxes for Stable Zn-Metal Anodes. *Adv. Mater.* **2022**, *34*, e2200342. [CrossRef]

41. Sun, H.; Huyan, Y.; Li, N.; Lei, D.; Liu, H.; Hua, W.; Wei, C.; Kang, F.; Wang, J.G. A Seamless Metal-Organic Framework Interphase with Boosted Zn(2+) Flux and Deposition Kinetics for Long-Living Rechargeable Zn Batteries. *Nano Lett.* **2023**, *23*, 1726–1734. [CrossRef] [PubMed]

42. Chen, P.; Yuan, X.; Xia, Y.; Zhang, Y.; Fu, L.; Liu, L.; Yu, N.; Huang, Q.; Wang, B.; Hu, X.; et al. An Artificial Polyacrylonitrile Coating Layer Confining Zinc Dendrite Growth for Highly Reversible Aqueous Zinc-Based Batteries. *Adv. Sci.* **2021**, *8*, e2100309. [CrossRef]

43. Zhong, Y.; Xu, X.; Liu, P.; Ran, R.; Jiang, S.P.; Wu, H.; Shao, Z. A Function-Separated Design of Electrode for Realizing High-Performance Hybrid Zinc Battery. *Adv. Energy Mater.* **2020**, *10*, 2002992. [CrossRef]

44. Qin, R.; Wang, Y.; Zhang, M.; Wang, Y.; Ding, S.; Song, A.; Yi, H.; Yang, L.; Song, Y.; Cui, Y.; et al. Tuning Zn2+ coordination environment to suppress dendrite formation for high-performance Zn-ion batteries. *Nano Energy* **2021**, *80*, 105478. [CrossRef]

45. Yi, J.; Liang, P.; Liu, X.; Wu, K.; Liu, Y.; Wang, Y.; Xia, Y.; Zhang, J. Challenges, mitigation strategies and perspectives in development of zinc-electrode materials and fabrication for rechargeable zinc–air batteries. *Energy Environ. Sci.* **2018**, *11*, 3075–3095. [CrossRef]

46. Qi, C.; Weinell, C.E.; Dam-Johansen, K.; Wu, H. Assessment of Anticorrosion Performance of Zinc-Rich Epoxy Coatings Added with Zinc Fibers for Corrosion Protection of Steel. *ACS Omega* **2023**, *8*, 1912–1922. [CrossRef]

47. Qiu, M.; Jia, H.; Lan, C.; Liu, H.; Fu, S. An enhanced kinetics and ultra-stable zinc electrode by functionalized boron nitride intermediate layer engineering. *Energy Storage Mater.* **2022**, *45*, 1175–1182. [CrossRef]

48. Zhu, M.; Hu, J.; Lu, Q.; Dong, H.; Karnaushenko, D.D.; Becker, C.; Karnaushenko, D.; Li, Y.; Tang, H.; Qu, Z.; et al. A Patternable and In Situ Formed Polymeric Zinc Blanket for a Reversible Zinc Anode in a Skin-Mountable Microbattery. *Adv. Mater.* **2021**, *33*, e2007497. [CrossRef]

49. Michlik, T.; Rosin, A.; Gerdes, T.; Moos, R. Improved Discharge Capacity of Zinc Particles by Applying Bismuth-Doped Silica Coating for Zinc-Based Batteries. *Batteries* **2019**, *5*, 32. [CrossRef]

50. Yu, F.; Shah, A.; Leung, P. A numerical model of a zinc-para-benzoquinone membrane-free organic flow battery. *Energy Rep.* **2022**, *8*, 1158–1165. [CrossRef]

51. Zhang, P.; Liu, X.; Fu, J.; Chu, F. Mass Transfer Behaviors and Battery Performance of a Ferrocyanide-Based Organic Redox Flow Battery with Different Electrode Shapes. *Energies* **2023**, *16*, 2846. [CrossRef]

52. Jiang, Q.; Lu, H.M. Size dependent interface energy and its applications. *Surf. Sci. Rep.* **2008**, *63*, 427–464. [CrossRef]
53. Roeber, E.F.; Parmelee, H.C. *Electrochemical and Metallurgical Industry*; Electrochemical Publishing Company: Pennington, NJ, USA, 1907.